Ionics (2025) 31:12619–12637
https://doi.org/10.1007/s11581-025-06753-9

RESEARCH

Binder formulation and microstructure in very high loading 3D-printed $LiFePO_4$ electrodes

Tú T. T. Nguyen[1,2,3] · Hamid Hamed[2,3] · Jan D'Haen[2,4] · Yoran De Vos[1,3] · An Hardy[2,3,4] · Sébastien Sallard[1,3] · Jasper Lefevere[1,3] · Mohammadhosein Safari[2,3,4]

Received: 8 April 2025 / Revised: 19 June 2025 / Accepted: 29 September 2025 / Published online: 13 October 2025

Abstract
3D-printing has emerged as a promising method for the fabrication of high loading electrodes to increase the energy density of the lithium-ion batteries (LIBs). The formulation and preparation of the printing inks, however, are not trivial and have a significant impact on the electrochemical and structural properties of the 3D-printed electrodes. Here, a comprehensive investigation is conducted to quantify the impact of binder formulation on the performance of the 3D-printed lithium iron phosphate (LFP) electrodes with active-material loadings beyond 25 mg/cm^2. This is showcased with the commonly used binders of carboxymethyl cellulose (CMC) and poly(3,4-ethylenedioxythiophene):polystyrene sulfonate (PEDOT:PSS) and by highlighting their impact on the printability, microstructure, and cycling behavior of the LFP electrodes made thereof. To do so, a combination of the electrochemical and microstructural characterization techniques is employed to reveal the synergistic effect of the CMC and PEDOT:PSS binders on the mechanical integrity, electrical conductivity, tortuosity, and cycling performance of the 3D-printed LFP electrodes. The results underscore the significance of the binder in optimizing the 3D-printing process for the manufacturing of the energy-dense electrodes.

Keywords 3D-printing process · Energy-dense electrodes · Carboxymethyl cellulose

Introduction

In the quest for advanced energy storage solutions, the combination of state-of-the-art 3D printing technology and lithium-ion batteries (LIBs) has sparked a new wave of innovation: thick electrodes with enhanced energy density. The LIBs made with electrodes of high active material loading need fewer inactive components such as separator and current collector and thus enable reaching higher values of energy density at the cell level [1–4]. For instance, it is estimated that the energy density of an LIB can be raised 30% by increasing the electrode thickness from 25 to 200 μ m [2]. Nevertheless, it is not feasible to fabricate such thick electrodes using the conventional coating techniques from which the produced thick electrodes often suffer from delamination at the electrode-current collector interface and exhibit poor mechanical integrity [5].

The conventional techniques like the slot-die or doctor-blade are highly prone to result in electrodes with higher tortuosity inducing significant limitations for the charge transport and rate performance of the battery [6, 7]. Great attention has been recently directed to 3D-printing, sometimes referred to as additive manufacturing, as an alternative coating technique for battery electrodes [8]. The 3D-printing technology facilitates the fabrication of porous electrodes by regulating the spatial arrangement of the electrode fibers to create an optimal ionic percolation network that uniformly extends throughout the whole volume of a thick electrode (Fig. 1). Additionally, the potential higher uniformity in the distribution of the components in the 3D-printed electrodes can reinforce the mechanical integrity [5].

In recent years, direct-ink-writing (DIW) 3D printing techniques have been widely used to fabricate LIBs, thanks to their flexibility in structural design and facile

---

✉ Mohammadhosein Safari
momo.safari@uhasselt.be

[1] VITO (Flemish Institute for Technological Research), Sustainable Materials, Mol 2400, Belgium

[2] Institute for Materials Research (IMO-Imomec), UHasselt, Martelarenlaan 42, Hasselt B-3500, Belgium

[3] Energyville, Thor Park 8320, Genk B-3600, Belgium

[4] IMEC Division IMOMEC, Diepenbeek 3590, Belgium

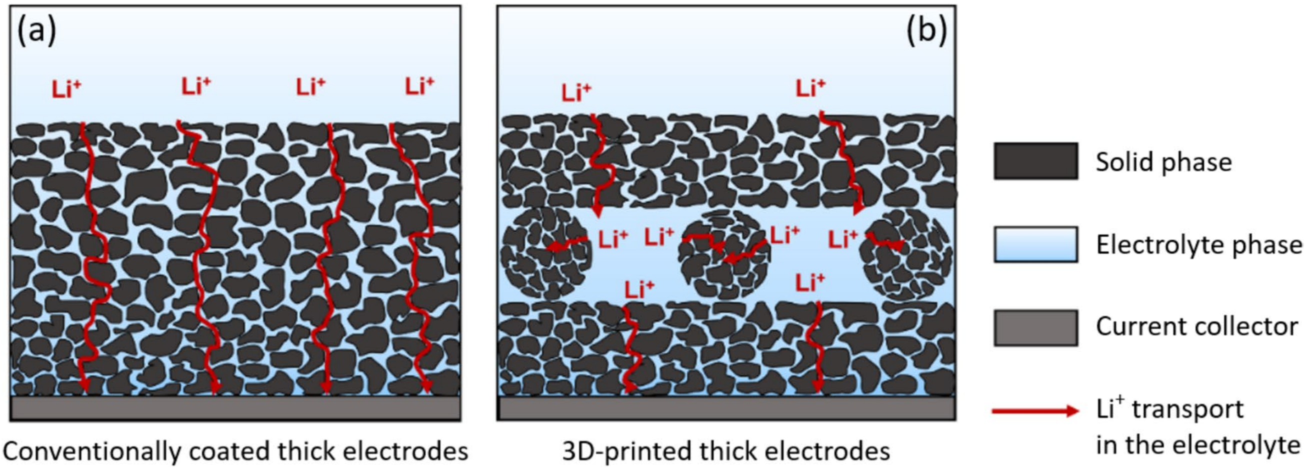

Fig. 1 Distinct arrangments of solid and electrolyte phases in the thick electrodes prepared by **a** conventional coating methods (e.g., doctor blade) and **b** 3D printing

manufacturing of LIBs onto various substrates. [9, 10]. There are growing number of reports on the application of inexpensive DIW methods to print battery components including separator [11, 12], electrolyte [13–15], cathode [16–19], and anode [20–23]. These techniques impose stringent requirements on the rheological properties of the printing inks. How smoothly the inks flow and whether the printed fibers can retain their shape after the printing primarily relies on the formulation and rheological behavior of the ink [24]. In this regard, binder is a key component in defining the flow characteristics of the printing ink [25]. Through a strategic selection and formulation of binder, one can control ink's rheological parameters such as viscosity, thixotropy, and shear thinning to ensure an optimal DIW 3D-printing process.

Despite their insignificant mass fraction in the LIBs' electrodes, binders play a vital role in the battery performance evidenced by extensive research on the electrodes coated with conventional techniques. The binder acts as an adhesive agent to agglutinate active material, conductive additives, and the current collector while ensuring a homogeneous dispersion of the electrode components [26–28]. Moreover, binders influence the tortuosity of the electrodes [29, 30] and hence the rate capability and cycling stability [31, 32] of the LIBs. There is, however, limited knowledge on the impact of binder formulation on the microstructural details of the 3D-printed LIB electrodes [33].

The carboxymethyl cellulose (CMC) is an aqueous, cost-effective, and environmental-friendly binder material known as an alternative to PVDF for LIBs [34–37]. In 2017, Liu et al. successfully fabricated 3D-printed ultrathick LFP electrodes formulated by CMC and LFP loading of 4.0 mg using DIW at low temperatures [38]. The polystyrene sulfonate (PEDOT:PSS) is an electronically conductive binder which has been demonstrated beneficial to the battery performance when used standalone and in combination with CMC [39–43].

In 2020, Eliseeva et al. showcased the constructive synergistic impact of CMC and PEDOT:PSS binders on the rate capability and capacity retention of the LFP electrodes [39]. In the following year, Bao et al. reported the successful fabrication of thick electrodes containing PEDOT:PSS and CMC binders using 3D-printing technology [33]. Although the authors did not compare the battery performance between the 3D-printed electrodes made from the CMC + PEDOT:PSS and CMC formulations, they mentioned the added value of PEDOT:PSS to the printability and electrical conductivity of the CMC-based LFP inks. There is, however, no comprehensive report in the literature about the impact of CMC and PEDOT:PSS binders when used individually and in combination on the printability and battery performance of thick 3D-printed LFP electrodes. Particularly, there are limited reports (Table S1) on high areal loading the 3D-printed LFP electrodes (> 20 mg/cm^2) and formulated with inks rich in LFP (> 90% wt.%).

Here, a comprehensive investigation of the 3D-printed thick LFP electrodes is presented, with a focus on binder composition in the printing ink. A series of LFP electrodes are printed with two different types of binders (CMC and PEDOT:PSS) and two different sizes of LFP particles. These electrodes are then studied to understand the impact of the ink formulation and composition on the printability and shape retention as well as the morphological, microstructural, and electrochemical properties of the resulting electrodes.

Table 1 Formulation of the LFP dry electrodes and solid proportion in the corresponding wet inks used for the 3D printing

Ink identifier	LFP source*	LFP loading (mg/cm^2)	Thickness (µm)	Composition of the dry LFP electrodes LFP/CB/CMC/PEDOT:PSS (wt%—vol%)	Solid fraction in the wet printing/coating ink (wt%)
4CMC	#1	58.3 ± 0.5	400 ± 3.2	94/2/4/0–63.5/30.4/6.1/0	60.9
4PEDOT	#1	32.1 ± 0.8	400 ± 1.1	94/2/0/4–61.4/29.4/0/9.2	53.4
2CMC _2PEDOT	#1	47.1 ± 1.7	400 ± 2.5	94/2/2/2–62.4/29.9/2.9/4.8	51.7
4CMC _2PEDOT	#1	27.1 ± 1.9	400 ± 1.4	92/2/4/2–60.0/29.4/5.9/4.7	52.6
4CMC _2PEDOT_DB	#1	24.7 ± 0.3	170 ± 1.3	92/2/4/2–60.0/29.4/5.9/4.7	22.6
4CMC_2PEDOT*	#2	26.5 ± 0.3	400 ± 1.5	92/2/4/2–60.0/29.4/5.9/4.7	52.1
4CMC_2PEDOT_8CB*	#2	23.9 ± 0.3	400 ± 1.5	86/8/4/2–30.4/63.9/3.2/2.5	43.8
4CMC_2PEDOT_thin*	#2	18.1 ± 0.2	270 ± 1.2	92/2/4/2–60.0/29.4/5.9/4.7	52.1
4CMC_2PEDOT_DB*	#2	25.4 ± 0.3	172 ± 0.8	92/2/4/2–60.0/29.4/5.9/4.7	19.6
4CMC_2PEDOT_8CB_DB*	#2	22.1 ± 0.5	210 ± 0.9	86/8/4/2–30.4/63.9/3.2/2.5	13.6
Properties of LFP powders			**LFP #1**	**LFP #2**	
Particle size (nm)			~ 375	~ 100	
BET surface area (m^2/g)			12.21	10	
Type			No agglomerate	Agglomerate	
Carbon content (wt.%)			1.3	1.7	

Experimental and methods

Different series of 3D-printed and doctor blade-coated electrodes were prepared for this study. These electrodes were used in two main groups of investigations. The first category of electrodes was designed and prepared for a comprehensive study of the link between the binder formulation and the microstructural attributes and the electrochemical performance of the Li/LFP cells made thereof. To do so, a base LFP powder (LFP#1) was used to prepare four different series of ink formulations to coat the LFP electrodes with an overall binder weight percentage of 4 or 6%. These electrodes are hereafter named according to the binder composition (Table 1).

The 4CMC and 4PEDOT represent the LFP electrodes formulated with a 4 wt.% single binder of CMC and PEDOT:PSS, respectively. The 2CMC_2PEDOT and 4CMC_2PEDOT electrodes contain both the CMC and PEDOT:PSS binders with 2:2 and 4:2 fractions, respectively. All the electrodes were coated with a 3D printer except for the 4CMC_2PEDOT_DB which was prepared with a conventional doctor-blade technique to serve as a reference. The second category of the electrodes were prepared based on a single binder formulation "4CMC_2PEDOT" to conduct a primary analysis on the sensitivity of the rate performance of the 3D-printed electrodes to the properties of the LFP raw material and its areal loading. To do so, a second batch of LFP powder (LFP#2) was used. In this group, the identifier of the electrodes ends with a star sign (*, see Table 1).

Materials

The LFP powder was purchased from two different sources. LFP#1 was purchased from Xiamen Tob New Energy Technology Co. LTD., China, and the LFP#2 was purchased from Johnson Matthey. The properties of these powders, according to the data sheets, are compared in Table 1. The conductive carbon black C-Nergy Super C-45 (CB) provided by Imerys, with the particle size ~ 100 nm. The commercialized carboxymethyl cellulose (CMC, Mw = 250,000, DS = 0.9) was supplied by Sigma-Aldrich and the polymeric binder Poly(3,4-ethylenedioxythiophene) polystyrene sulfonate (PEDOT:PSS, ratio 1:1) 5% aqueous solution was provided by Agfa. Carbon-coated aluminum foil was purchased from PI-KEM.

Ink preparation and electrode coating

A highly viscous ink for DIW 3D-printing was prepared by stepwise addition of LFP and CMC powder mixture into the suspension of PEDOT:PSS, CB, and deionized water. First, the sieved carbon black CB was dispersed into deionized water, followed by the addition of PEDOT:PSS aqueous solution (depending on the formulation). To ensure a homogeneous dispersion, the suspension was primarily mixed in a Thinky mixer for 2 min at 2000 rpm, and sonicated for 20 min at room temperature. The LFP and CMC were dry mixed and then dispersed into the sonicated suspension stepwise. A mixing program of 2 min at the speed of 2000 rpm at each step was applied to obtain a homogeneous viscous ink. Once the inks were ready, they were loaded into a cartridge and brought to an in-house 3D printer for the DIW process [44].

The 3D-printing was conducted in a temperature- and humidity-controlled environment (20 °C, 80% RH) to ensure consistency in the ink rheology and printing conditions. A viscoelastic ink was 3D-printed in a layer-by-layer fashion through a 200-μm nozzle (flow rate 35 μL/min, printing speed 38 mm/s) to generate coin-shape LFP electrodes. Typically, a small nozzle is desirable to 3D-print electrodes for Li-ion batteries, as it directly results in shorter diffusion lengths within the fibers. For this reason, a 200 μm nozzle was used in our work. To the best of our knowledge, there are limited reports that managed to 3D-print electrodes using a 200 μm nozzle, but rather employing one with a size greater than 250 μm [18, 33, 38, 45–47].

The design of the electrodes was programmed as follows: a 3-layered circular structure with a diameter of 15 mm, the center-to-center distance between two fibers at 350 μm in each layer, and an angle of 90° between each layer. The LFP electrodes were printed on paper, which was removed after the electrodes were dried in a vacuum oven overnight at room temperature. The dried stand-alone 3D-printed electrodes were immediately weighed and transported to an antechamber, where they were dried under the vacuum condition at 50 °C for 2 h before entry to the Argon-filled glovebox (Jacomex GP-concept) for coin cell assembly.

Inks with lower viscosity were prepared for the doctor-blade coating of the LFP electrodes on the C-coated aluminum foils. Despite the higher solvent content of the low viscosity ink for doctor blade coating compared to that of high viscosity ink for 3D-printing, the dried electrodes prepared from the two fabrication methods share similar solid compositions after solvent evaporation. The LFP and CMC powders were pre-mixed before being dispersed into the sonicated suspension of CB, PEDOT:PSS, and deionized water to acquire homogeneous slurries. As the slurries were much less viscous than the printing inks, the stepwise mixing was run for 5 min at the speed of 2000 rpm per step to ensure homogeneity, followed by a defoaming program for 5 min at 2000 rpm to eliminate the air bubbles from the slurries. Next step involved tape-casting the slurry onto a carbon-coated aluminum foil to obtain 170-μm-thick electrodes, with a similar average LFP loading to their 3D-printed counterparts (~ 24.7 mg/cm^2).

The electrodes were assembled into the coin cells following the same processes (e.g., drying) similar to the 3D-printed electrodes. For some selected samples, the impact of the drying condition was investigated by preparation of the 3D-printed electrodes using different drying protocols. In the standard protocol, the electrodes were dried under vacuum at 25 °C for 18 h. Once dried, the electrodes were weighed and transferred into an antechamber, where they were under vacuum at 50 °C for 2 h before being brought into the glovebox for cell assembly. In the freeze-drying protocol, the electrodes were subjected to vacuum freeze-drying for 18 h. After that, they were further dried in a vacuum oven at 25 °C for another 18 h before being brought into the glovebox.

Characterization of the ink and porous electrodes

Rheology of the highly viscous inks and lowly viscous slurries were investigated at 25 °C using a HAAKE MARS 60 (Thermo Fisher) with a 20-mm plate-plate geometry and under oscillatory and rotational modes. During the measurements, the gap between the two plates was maintained at 0.4 mm and a solvent trap was used to prevent solvent evaporation. Details on the linear viscoelastic range and cross-over point G'-G'' were provided by oscillatory measurements, while rotational measurements provided insights into the yield stress and shear viscosity. In the oscillatory measurement, the shear storage modulus (G') was recorded for a shear stress range of 0–10,000 Pa at 1 Hz. In the rotational measurement, during the first 300 s, the shear rate was increased from 0.01 to 100 s^{-1} and then decreased back to 0.01 s^{-1}.

Optical images of the 3D-printed electrodes were captured using a ZeissDiscovery V12 stereomicroscope, equipped with a Plan Apo S 1.0xFWD 60 mm objective. The images were processed with the Axio Vision software to estimate the fiber diameter and inter-fiber distances. The scanning electron microscopy (SEM) images of the electrodes were obtained using a FET™ Nova Nano SEM 450 (FEI, USA) at 5-kV acceleration voltage in secondary electron imaging mode. An Autosorb iQ2 (Quantachrome) volumetric sorption analyzer was used to characterize the porous structure of the samples. To do so, samples were degassed at 200 °C for 16 h under vacuum condition before performing the N_2-physisorption measurements at 77 K.

To approximate the electronic bulk resistance, the electrodes were placed between two stainless steel spacers and subsequently assembled within a standard CR2025 coin-cell without the addition of any electrolyte. The resistance of the cell was then measured using a Keithley source. The details about the sheet resistance and tortuosity measurements are provided in the supporting information document.

Battery assembly and cycling tests

The prepared LFP electrodes (15 -mm diameter) and a Li metal disc (16-mm diameter) were used to assemble the CR2032 coin cells inside the glovebox. A polymeric thin film (Celgard 2400, 19-mm diameter) was positioned between the two electrodes as a separator. This separator was soaked with 200 µl of an electrolyte with a formulation of lithium hexafluorophosphate ($LiPF_6$) 1 M in a mixture of ethylene carbonate (EC) and dimethyl carbonate (DMC) 50/50 in weight proportion (SoulBrain MI). The coin cell was sealed by a pneumatic press inside the Ar-filed glove box. The cycling and impedance measurements at 25 °C were conducted by the Bio-Logic BCS-810 setup.

The battery tests started with a rest period at an open-circuit voltage (OCV) for 6 h before the current was applied to insure a homogenous wetting of the cells. Different tests were performed in a voltage range of 2.5–4.1 V vs. Li^+/Li, either long-term cycling at C/10 or rate capability testing at C/20, C/10, C/5, C/2, 1 C, and C/20 with 5 cycles run at each C-rate. For the electrochemical impedance spectroscopy (EIS) experiments, a perturbation amplitude of 10 mV around OCV and a frequency range of 10 kHz–10 mHz was used. Note that 1C-rate is defined as the current density to fully (dis)charge the LFP electrodes within 1 h based on the theoretical specific capacity of the LFP, i.e., 1 C is equivalent to a current 169.9 mA/g_{LFP}. For the post-mortem analyses, the disassembly of the cycled cells was operated inside the Ar-filled glovebox to collect the cycled electrode, which was then placed on a SEM holder and brought into a transfer module CT0-0 (Kammrath Weiss Gmbh) for SEM analysis.

Results and discussions

Rheology and 3D printing

The printability of the printing inks was investigated by the rotational and oscillatory rheological tests (Fig. 2, Table 2). First, the rotational measurement (also known as thixotropy loop) was conducted to understand the flow behavior of the inks and to determine their suitability for DIW. In this measurement, the printing ink is applied between two plates and the top plate is rotated with increasing shear rate (speed) while the shear stress (torque) is measured and thus the viscosity of the paste is evaluated with increasing shear rate. Afterward, the shear rate is reduced again, while measuring the resulting shear stress, and corresponding viscosity. The results obtained in this measurement give an indication of the general rheological behavior of the printing inks, and the viscosity of the inks under high flow (indicative of the flow when being extruded through the printing nozzle [24]) and the viscosity of the inks under low flow (indicative of the

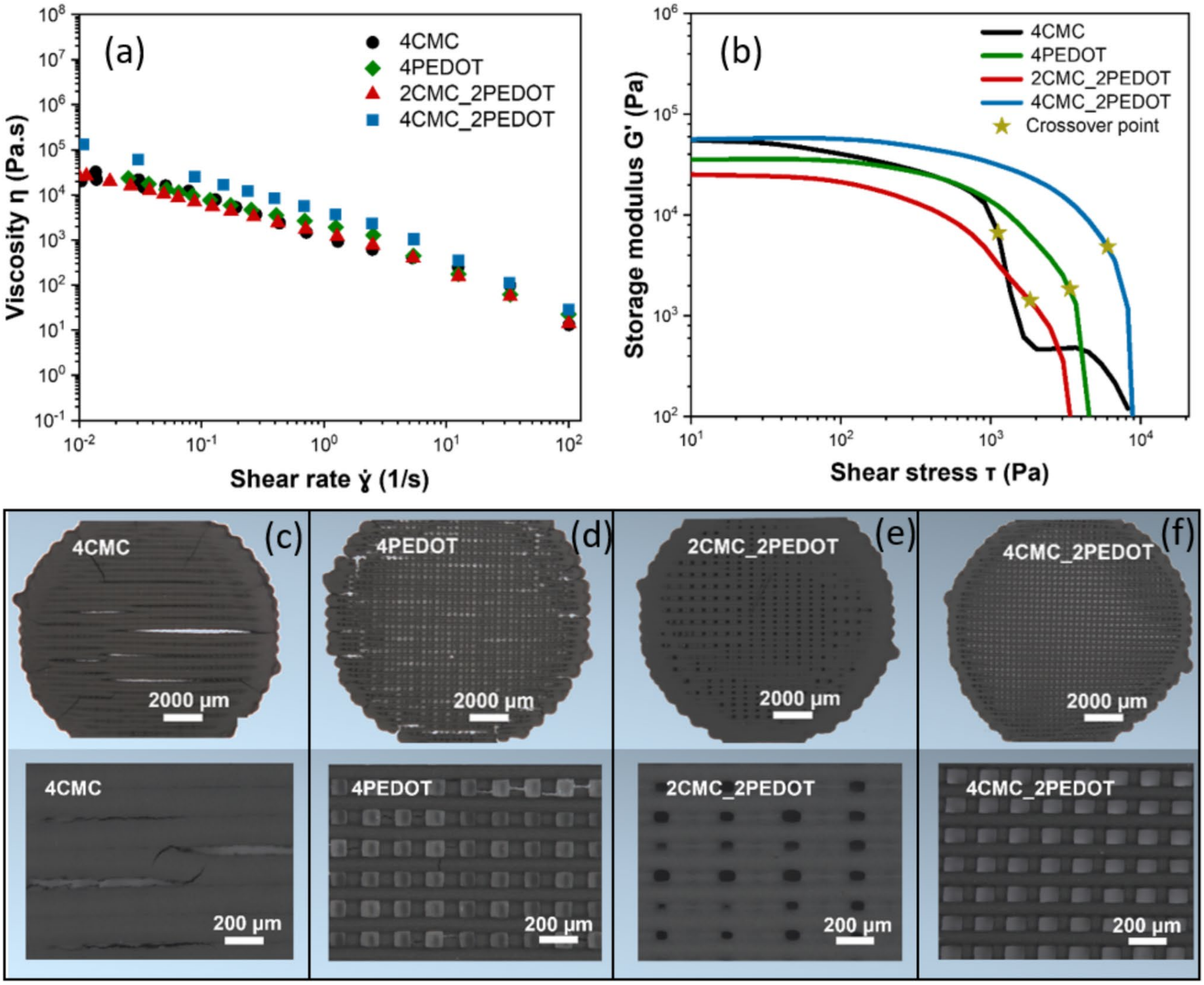

Fig. 2 Rheological properties of the investigated LFP inks 4CMC (94 wt.% LFP, 2 wt.% CB, and 4 wt.% CMC), 4PEDOT (94 wt.% LFP, 2 wt.% CB, and 4 wt.% PEDOT:PSS), 2CMC_2PEDOT (94 wt.% LFP, 2 wt.% CB, 2 wt.% CMC, and 2 wt.% PEDOT:PSS) and 4CMC_2PEDOT (92 wt.% LFP, 2 wt.% CB, 4 wt.% CMC, and 2 wt.% PEDOT:PSS) **a** apparent viscosity as a function of increasing shear rate and **b** storage modulus as a function of shear stress. **c–f** the optical microscope top-view images of the dry 3D-printed electrodes at different magnifications

Table 2 Details on the rheology of the investigated inks and the resulting structure of the dried 3D-printed LFP electrodes

Ink identifier	Rheology			3D-printed structure			
	G'$_{LVR}$ (10^4 Pa)	τ_{flow} (10^3 Pa)	η (Pa·s)	LFP loading (mg/cm^2)	d_{fiber} (µm)	r_{fiber} (µm)	$d_{inter\text{-}fiber}$ (µm)
4CMC	4.8	1.1	113	58.3 ± 0.5	333 ± 3.2	166.5 ± 1.6	≈ 0
4PEDOT	3.5	3.3	460	32.1 ± 0.8	154 ± 1.0	77 ± 0.5	197 ± 1.3
2CMC_2PEDOT	2.4	1.8	361	47.1 ± 1.7	280 ± 2.9	140 ± 1.5	81 ± 2.7
4CMC_2PEDOT	5.7	6.0	352	27.1 ± 1.9	144 ± 0.6	72 ± 0.3	185 ± 0.5

flow characteristics after printing). In printing inks, typical shear thinning behavior is observed [48]. These inks typically have particles or binders inside, resulting in the buildup of an internal network structure at a low shear rate.

When the shear rate surges during the measurement, the internal structure of the ink is broken down, and the viscosity decreases (shear thinning behavior). During the second step, the shear rate is reduced resulting in an increase in viscosity because of the recovery of the interparticle interactions inside the ink [24, 49]. This network recovery is the main initial mechanism of solidification of the printing inks in DIW before potential further treatment. As such, the thixotropy loop gives some information on the breakdown and recovery of the interparticle interactions in the ink under the extrusion pressure through a small nozzle [24, 49].

All the prepared inks showed the previously mentioned shear-thinning behavior required for direct ink writing (Fig. 2a) [50, 51]. Such behavior confirms the flowability of the ink when exiting the nozzle [24]. The viscosity of the inks at a shear rate of 1 s^{-1} during the recuperation branch is listed in Table 2 to give an indication of the shape retention characteristics of the printing inks after printing. This data shows that the ink containing only 4 wt.% CMC (4CMC) with a relatively low viscosity value ($\eta = 113$ Pa·s) might struggle to keep its recovered gel network after printing while the other inks have a significantly higher viscosity value, above 350 Pa·s.

After this thixotropy loop, also oscillatory measurements were conducted to better evaluate the network structure and viscoelastic properties of the printing inks. During the amplitude sweep measurement, the printing ink was placed in between two plates, and the plates were oscillated with an increasing stress (and increasing amplitude), while evaluating the storage (G’) and loss (G’’) moduli in function of the applied shear stress. The storage modulus (G’) represents the elastic characteristic while the loss modulus (G’’) illustrates the viscous behavior of the ink [24].

At very low shear stresses, G’ is larger than G’’, because the internal network inside the printing paste is kept intact, and the ink exhibits “solid-like” behavior (Fig. S1). When slightly increasing the applied shear stress, the G’ and G’’ values remain constant as long as the ink is in its linear viscoelastic region (LVR). The length of this LVR shows how far the internal structure of the printing ink can be deformed before the onset of internal structure breakdown. The storage modulus at the LVR (G'_{LVR}) reflects the rigidity of the printing ink and its ability to retain the shape after the extrusion. When the stress is further increased after structural breakdown, at some point the loss modulus crosses and becomes higher than the storage modulus (G’ = G’’), also called crossover point, which indicates the printing ink becoming more ‘liquid-like. When this crossover point occurs at a higher shear stress, this indicates a higher stress requirement to initiate flow.

Figure 2b illustrates the storage modulus (G’) behavior of the different inks before and after the cross-over point (star markers in Fig. 2b), where the ink transitions from solid- to liquid-like behavior occurs under the shear stress (τ_{flow}). Table 2 includes the storage modulus at the LVR and the stress at which the crossover point occurs. The LFP inks formulated with 4 wt.% CMC, including 4CMC and 4CMC_2PEDOT have a higher storage modulus at the LVR (Table 2, Fig. 2b), indicating a fairly strong and rigid internal network structure. Moreover, the data suggests that the LFP ink with 2 wt.% CMC and 2 wt.% PEDOT yield the least rigid 3D-printed structures on account of lower G'_{LVR}. 4CMC_2PEDOT and 4PEDOT show a relatively long LVR (Fig. 2b) and correspondingly higher stress at the crossover point (Table 2) indicating a higher stability of the printed structures against flow. As such, a good shape retention can be expected for 4CMC_2PEDOT and 4PEDOT while fine 3D-printed structures of 2CMC_2PEDOT and 4CMC might not be realized due to their inferior rheological properties.

The inks were 3D-printed at room temperature and dried before further characterization (Fig. 2c). The 4CMC electrode exhibits inter-fiber cracks across multiple fibers due to the fast drying at room temperature. The 4CMC electrodes exhibit a relatively diffuse structure in which the target 3D pattern is not visible (Fig. 2c). The fiber diameter is 333 ± 3.2 μm which is much larger than the expected size of 200 μm and the inter-fiber distance is too small to be quantified (Table 2). This observation is in line with the low viscosity of the 4CMC inks resulting in a poor retention of the original structure after the micro-extrusion.

The 4PEDOT electrodes show intra-fiber cracks and are fragile after vacuum drying due to the poor mechanical strength of each individual fiber (Fig. 2d). It is noteworthy that vacuum-conditioned drying was necessary for the 4PEDOT electrodes and those formulated with PEDOT:PSS. In these electrodes, the hygroscopic PSS in the ink promotes the absorption and retention of the moisture [52]. In the electrodes formulated with a combination of CMC and PEDOT:PSS, the inter- and intra-fiber cracks are absent (Fig. 2e-f). The results suggest that the synergistic beneficial impacts of the CMC and PEDOT:PSS on the mechanical integrity and shape retention of the 4CMC_2PEDOT electrodes, respectively (Fig. 2f).

According to rheological data, the inks containing only 4 wt.% CMC (4CMC) have a low viscosity but high storage modulus at the LVR (G'_{LVR}). The low viscosity value suggests that the inks struggle to keep their recovered gel network after printing, which negatively affects the shape of 4CMC structures. However, thanks to the high G'_{LVR} value, the as-printed structures appear fairly strong and rigid. In contrast, the inks containing only 4 wt.% PEDOT:PSS (4PEDOT) possess a higher viscosity but a lower G'_{LVR} value compared to 4CMC inks. In effect, the 4PEDOT structures are better-shaped, but they also appear less strong and less rigid.

As CMC is combined with PEDOT:PSS as a binder mixture in 4CMC_2PEDOT ink, its viscosity and G'_{LVR} value of 4CMC_2PEDOT ink are improved compared to 4CMC and 4PEDOT inks. As such, the 3D-printed electrodes prepared from 4CMC_2PEDOT closely resemble the target

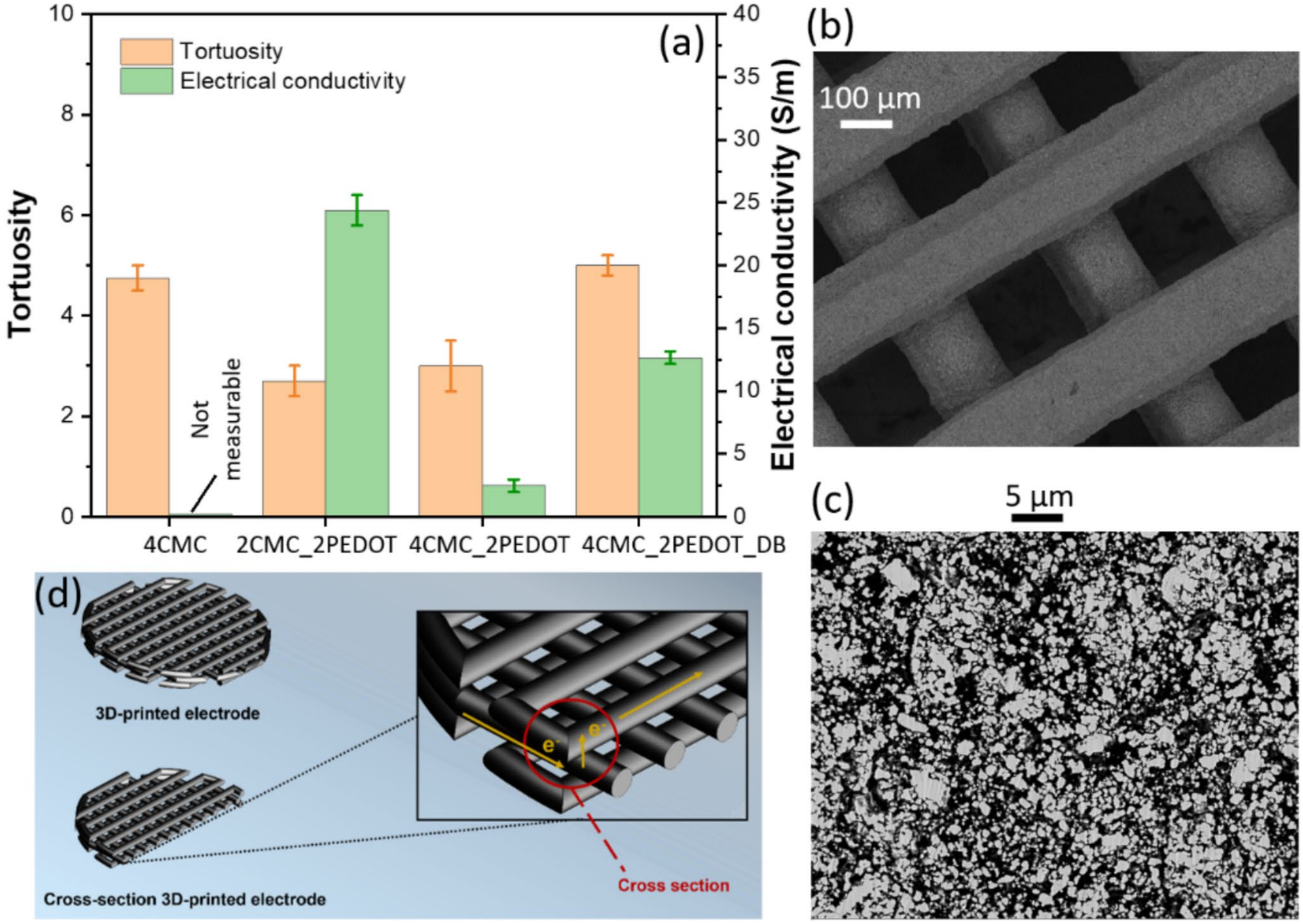

Fig. 3 **a** Tortuosity and electrical conductivity of the 3D-printed and doctor blade-coated LFP electrodes. The SEM images of a pristine 4CMC_2PEDOT LFP electrode **b** top view and **c** cross section of a fiber. **d** Graphical illustration of the electronic percolation network within a 3-layer 3D-printed LFP electrode of the present study (400 µm)

structure. Additionally, it should be pointed out that due to the less CMC content in the formulation and hence lower rigidity of the ink, the 2CMC_2PEDOT electrodes present a not as well-shaped structure.

The rheology of the inks formulated with a smaller particle size LFP#2 and with higher content of carbon black was also investigated. The results (Fig. S2) show that a reduced LFP particle size or higher content of carbon black will increase the apparent viscosity of the printing inks and can improve the shape retention of the 3D-printed electrodes. For example, we observed that the inks formulated with LFP#2 and higher concentration of carbon additive were too rigid to be flowable without the need for further dilution of the ink with water (Fig. S2a). To adjust their rheology and make them printable, additional water was added to the inks formulated with LFP#2 compared to the inks formulated

Table 3 Electronic sheet resistance and N_2-physisorption characteristics of the LFP electrodes

	4CMC	4PEDOT	2CMC_2PEDOT	4CMC_2PEDOT	4CMC_2PEDOT_DB
Sheet resistance (Ω/□)	NM	NM	128 ± 5	1231 ± 313	426 ± 17
Electrical resistivity (Ω·m)	NM	NM	0.041 ± 0.002	0.402 ± 0.088	0.079 ± 0.003
Electrical conductivity (S/m)	NM	NM	24.39 ± 1.2	2.48 ± 0.5	12.66 ± 0.5
BET (m^2/g)	15.7	66.4	28.1	27.9	47.3
Pore volume (ml/g)	0.029	0.075	0.049	0.052	0.074
Pore size (nm)	3.71	2.26	3.51	3.68	3.12

**NM*, not measurable

with LFP#1. As shown in Figure Fig. S2b, the diluted inks of 4CMC_2PEDOT_8CB* and 4CMC_2PEDOT* reached an apparent viscosity slightly higher than or comparable to the 4CMC_2PEDOT ink with LFP#1, making them suitable for 3D printing.

Despite dilution, 4CMC_2PEDOT_8CB* inks with 8 wt.% of carbon black exhibit longer LVR and higher G’LVR than inks with 2 wt.% of carbon black (4CMC_2PEDOT*) (Fig. S2c). A similar trend is observed when comparing inks formulated with LFP#2 to LFP#1 (Fig. S2c). The data confirms that increasing carbon black content or reducing LFP particle size can improve the shape retention of the 3D-printed electrodes.

Microstructural details of the LFP electrodes

The tortuosity and electronic conductivity of the LFP electrodes with different binder formulations are compared in Fig. 3a. The 4PEDOT electrodes were too fragile for the tortuosity, sheet resistance, and battery tests and therefore are excluded in the further discussions. Tortuosity of a porous electrode is an important property that provides insights into the ionic charge transport limitations within the electrodes [53]. Particularly, one of the main merits of the 3D-printing is to prepare the high-loading electrodes with lower tortuosity compared to what is possible with the conventional coating techniques.

The tortuosity of the 3D-printed 4CMC, 2CMC_2PEDOT, and 4CMC_2PEDOT electrodes lie in the range of 2.70–4.75 which is lower than the tortuosity of the doctor-blade coated 4CMC_2PEDOT_DB electrode. However, it is important to note that these tortuosity values are volume averaged and does not necessarily reflect the local variations. As such, although the through-plane transport of charge is considerably less limited and facilitated by the apertures of the 3D-printed structures (Fig. 1), but the intra-fiber transport can be still limited in case of high tortuous fibers. For instance, the 2CMC_2PEDOT has the lowest tortuosity value (2.70) which can be explained by its more diffuse structure compared to the 4CMC_2PEDOT electrode. Although the local measurement of the tortuosity is not trivial for a single fiber but the cross-section SEM of the fibers from the 4CMC_2PEDOT electrode reveals a very dense and tortuous microstructure (Fig. 1, Fig. S4). This is in line with the estimated porosity of a single fiber in the 4CMC_2PEDOT electrode which is only 28% being significantly lower than that of the doctor blade-coated electrode (52%). The results also disclose a considerably lower tortuosity in the 3D-printed electrodes containing PEDOT:PSS compared to those containing only CMC. This points out the negative impact of the CMC on the tortuosity of the investigated LFP electrodes.

N_2-physisorption measurements were conducted to provide more insights into the microstructure of the LFP electrodes (Table 3). Particularly, the porosity and surface area of the electrodes are expected to correlate with the electrochemically active surface area and as such can be used for a relative comparison between the electrochemical performance of the samples. The 4PEDOT electrodes have a significantly higher specific surface area (66.4 m^2/g) and total pore volume (0.075 ml/g) compared to the 4CMC-based electrodes with 15.7 m^2/g BET surface area and 0.029 ml/g pore volume. This observation suggests that the 4PEDOT binder has a better pore-forming characteristic relative to the CMC binder in our electrode formulations. This is supported by the N_2-physisorption data revealing a higher mesoporous volume in the electrodes with 4PEDOT binder. However, further works need to further investigate the reasons behind the added value of the 4PEDOT binder. For instance, we expect that the fractal dimension of the aggregates within the printing inks with the 4PEDOT is lower which results in a higher porosity of the electrodes after drying [54].

The 4CMC_2PEDOT_DB electrode has a higher surface area and pore volume compared to its 3D-printed counterpart which further reflects the very dense internal microstructure of the fibers for the 3D-printed electrodes. The SEM top view of the electrodes (Fig. S5) reveals further morphological differences between the CMC- and PEDOT:PSS-based electrodes. The binder network in the presence of PEDOT:PSS is more scattered and manifests in as an adhesive net for the LFP electrodes. It is well known that PEDOT:PSS has a core-shell structure, in which PEDOT and PSS act as the core and shell, respectively [55]. In the dried 4PEDOT 3D-printed electrodes, HSO_3 groups in PSS chains at the shell are held strongly together via intra- and inter-molecular hydrogen bonding, leading to formation of thin uniform PEDOT:PSS layer [56]. Unlike the core-shell structures in PEDOT:PSS, CMC chains are connected by intra- and inter-molecular hydrogen bonding via -OH functional group to create a network that binds LFP particles together [57].

The data shows that 2CMC_2PEDOT electrodes are more electronically conductive (24.39 S/m) than the 4CMC_2PEDOT electrodes (2.48 S/m). This highlights the detrimental effect of the insulating CMC on the electrical conductivity of the electrodes. The incorporation of PEDOT:PSS to the formulation leads to significant increase in the electrical conductivity of the electrodes, which is in line with the observation from Bao et al. [33] It is important to note that the four-point probe measurement did not work on 4CMC electrode samples due to the very low conductivity of the CMC. This was further corroborated by the electronic bulk resistance data of the

4CMC and 4CMC_2PEDOT electrodes (see supporting information). The results indicated that the bulk electronic resistance of the 4CMC electrode is significantly higher (400 Ω) than that of the 4CMC_2PEDOT electrode (30Ω). Moreover, the more diffuse pattern of the fibers in the 2CMC_2PEDOT relative to the 4CMC_2PEDOT electrodes leads to a better connectivity between the fibers which facilitates the electron transport throughout the electrode volume.

The doctor blade-coated 4CMC_2PEDOT electrode shows a higher electronic conductivity compared to its 3D-printed counterpart (Table 3). This can be attributed to the longer conduction pathways in the 400 µm thick 3D-printed electrodes compared to the 170-µm-thick doctor-blade electrodes. Particularly, the through-plane conduction is more limited in the 3D-printed design adopted in this work where the electrons need to first travel in-plane to the cross-section point between the two adjacent layers before a through-plane cross over between the layers (Fig. 3d). This observation highlights that the 3D patterns need to be optimized not only with respect to the ionic percolation but also the electronic network of the electrode.

In 2018, Wang et al. highlighted the influence of various designs of 3D-printed electrodes on the battery performance [16]. However, how these designs impact the tortuosity and electrical conductivity of their 3D-printed electrodes was not thoroughly reported. In our present work, it is clearly demonstrated that the grid-patterned 3D-printed structures are not as electrically conductive as their doctor blade-coated counterparts (Fig. 3a, Table 3). This can be attributed to

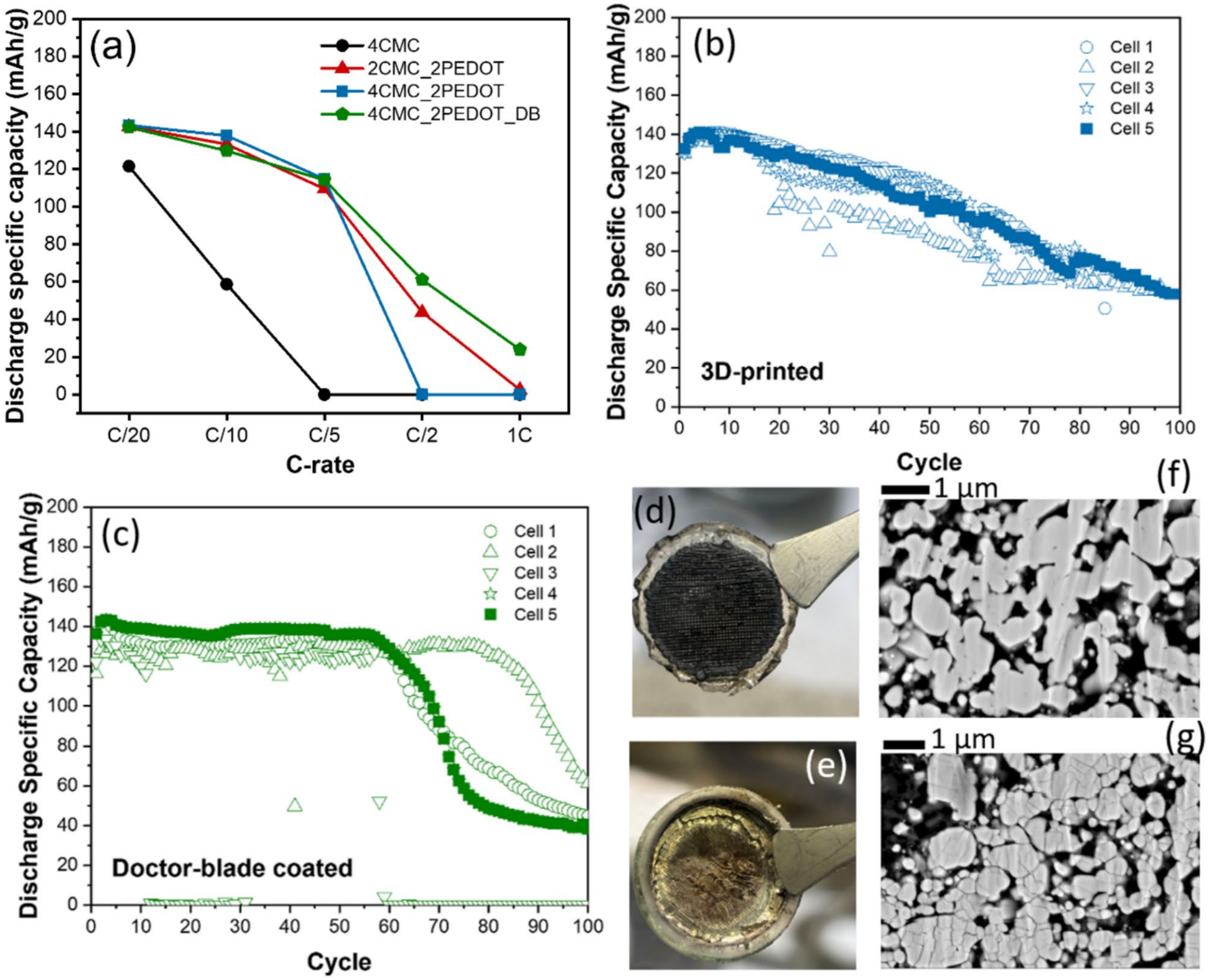

Fig. 4 **a** The rate capability of the Li/LFP cells with different 3D-printed and doctor blade-coated LFP electrodes. Cycling performance at C/10 of the **b** 4CMC_2PEDOT 3D-printed electrode (400 µm thick, 27.1 mg of LFP per cm2) and **c** doctor-blade 4CMC_2PEDOT_DB counterpart (170 µm thick, 24.7 mg of LFP per cm2). The optical image of the recovered **d** 4CMC_2PEDOT and **e** Li electrodes after long-term cycling. The SEM cross section of the 4CMC_2PEDOT electrodes **f** before and **g** after 100 cycles

the less contact area between the layers of materials in the 3D-printed structures compared to that of the traditional thick structures, leading to the slowdown of electron transport across the electrodes. Our observation is in line with the recent report of Miller et al. where they show that grid-patterned designs are not beneficial to the electron transfer kinetics of 3D-printed electrodes for sensing applications [58]. Our results highlight the significant impact of the configuration of the electronic percolation network on the effective conductivity of a porous electrode. The spatial distribution of the individual components of an electrode significantly impacts it's through- and in-plane conductivity. As such, it is expected that in a 3D-printed electrode with multiple layers, the establishment of an optimal through-plane percolation is very sensitive to the 3D pattern and the contact area between the different layers. This requires a careful optimization of the ink formulation as well as the 3D pattern of the electrode.

It is important to distinguish between the distinct physical and chemical properties of the PEDOT:PSS and CMC binders to better understand their impact on the printability and the electrical conductivity of the printing inks and the electrode performances reported in this study. The PEDOT:PSS is a conductive polyelectrolyte complex consisting of the polycation PEDOT and the polyanion PSS. It is noteworthy that PEDOT:PSS has a core-shell structure, with a PEDOT-rich core and a PSS-rich shell being held together by strong coulomb forces [59]. As a dry film, the PEDOT:PSS grains are connected by the hydrogen bonds between the sulfonate group of PSS. However, these hydrogen bonds get weakened in a moisture-rich environment [60], leading to the low storage modulus of PEDOT:PSS [61], which explains the low G' value and the weak mechanical strength of 4PEDOT ink and structures shown in Fig. 2.

CMC, on the other hand, can create a strong hydrogen-bonded network with water and other materials, thanks to the hydrophilic hydroxyl group from the cellulose backbone and the carboxymethyl group [62]. A study on the binding mechanism of CMC and graphitic particles shows that CMC forms a network to hold and bind the anode materials together [63]. This strong network between CMC and the active-material particles of an electrode enhances the overall mechanical integrity of the electrode. Furthermore, we reported the higher conductivity of 3D-printed structures formulated with PEDOT:PSS (2CMC_2PEDOT, 4CMC_2PEDOT) compared to those formulated with only CMC (4CMC) (Fig. 3a, Table 3). The conductive property of PEDOT:PSS stems from PEDOT, which has a conjugated π system in its thiophene rings that provides a pathway for electrons to move between individual particles [64]. On the contrary, CMC acts as an insulator due to the nature of its glucose backbone, explaining the low conductivity of 4CMC structures.

Battery performance

The short- and long-term performance of the Li/LFP coin cells assembled from the different LFP electrodes is summarized in Fig. 4. The rate capability of the 3D-printed electrodes containing PEDOT:PSS outperforms that of the electrodes containing only CMC (Fig. 4a, Fig. S6). 4CMC cells fail to cycle at C/5 while an average capacity of 115 mAh/g is delivered by the 2CMC_2PEDOT and 4CMC_2PEDOT cells at the same C-rate. The higher electrical conductivity and lower tortuosity of the 2CMC_2PEDOT electrodes enable them to sustain C/2 rate unlike the 4CMC_2PEDOT which are limited to the C/5. Overall, the 2CMC_2PEDOT cells outperform the 4CMC_2PEDOT cells with respect to the rate capability which is in line with the electrical conductivity and tortuosity of these samples (Fig. 3, Table 3). On the other hand, the doctor-blade coated 4CMC_2PEDOT_DB cells have a superior rate capability compared to the 3D-printed electrodes despite their inferior tortuosity. This highlights the significant share of the intra-fiber tortuosity in the polarization of the 3D-printed electrodes which limits their rate-capability and needs a dedicated investigation in the future works.

The electrochemical impedance spectroscopy (EIS) of the cells confirms the rate-capability data (Fig. S6−7). Particularly the charge-transfer resistance of the cells with 4CMC and 4CMC_2PEDOT_DB reads highest and lowest, respectively. The charge-transfer resistance is directly correlated to the electrochemically active surface area of the electrode. In this regard, the CMC has a negative impact on the effective surface area of the electrodes which is also in line with the insights gathered from the N_2-physisorption measurements (Table 3).

The long-term cycling of the 4CMC_2PEDOT and 4CMC_2PEDOT_DB electrodes at C/10 are compared in Fig. 4b, c. The data suggests that the Li/LFP cells with the 3D-printed electrodes have a better reliability in two aspects. First, the reproducibility of the aging dynamics is much higher for the 3D-printed electrodes relative to the conventionally coated electrodes. This is more evident when the best and worst performances recorded for the Li/LFP cells made from the two categories of 3D-printed and doctor blade-coated samples are compared against each another (Fig. 5). The evolution of the charge/discharge profiles and energy density of the 3D-printed electrodes exhibit much lower variance relative to the doctor-blade coated samples when the experiments are repeated during the reproducibility tests. This highlights the poor control over the microstructural details of the electrodes when a conventional doctor-blade technique is employed to prepare higher loading and thicker electrodes. Second, the capacity retention of the 3D-printed electrode is on average ~ 42% after 100 cycles. In contrast, the 4CMC_2PEDOT_DB electrodes have

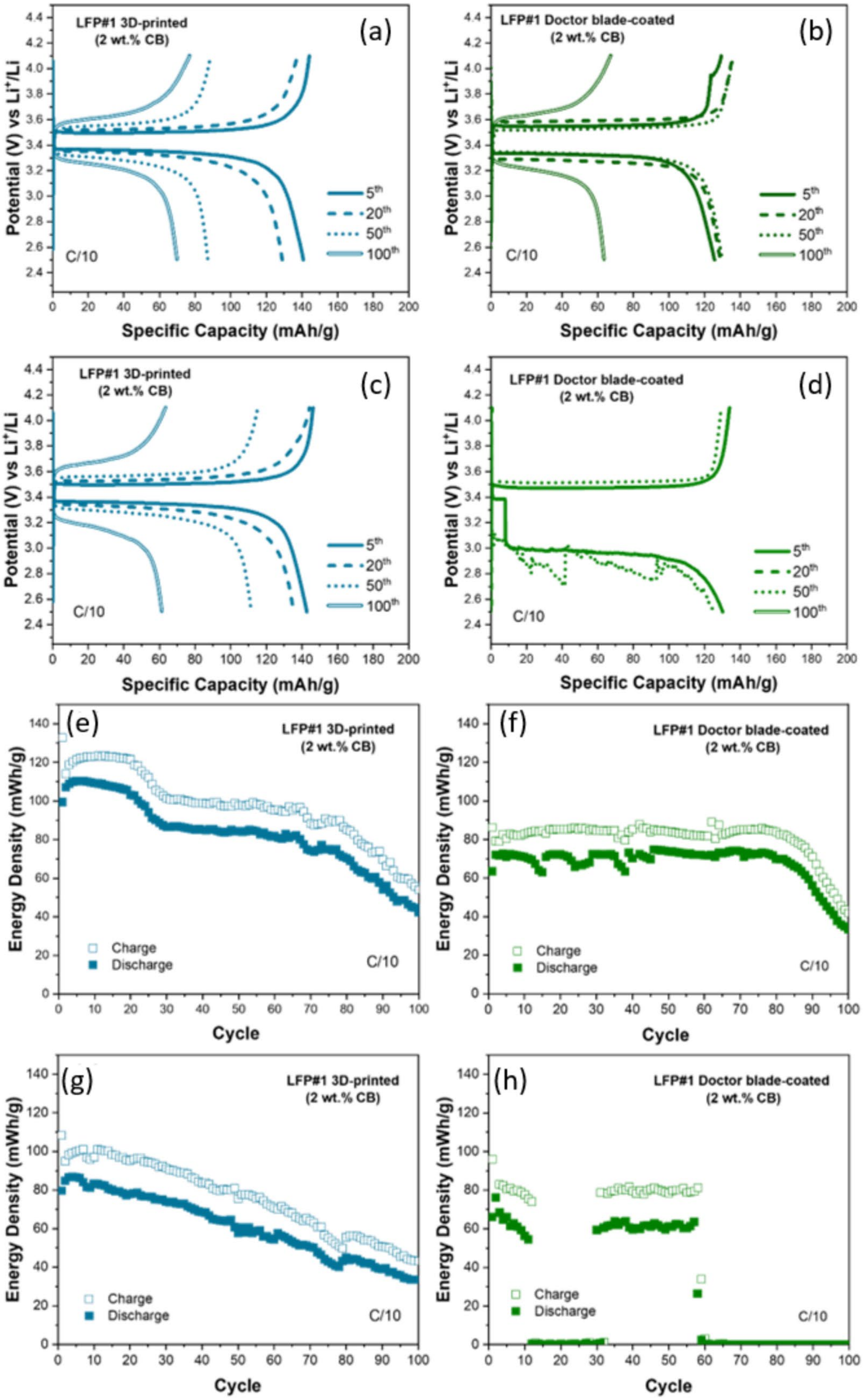
(a)
LFP#1 3D-printed
(2 wt.% CB)
C/10
5th
20th
50th
100th
Potential (V) vs Li+/Li
Specific Capacity (mAh/g)
(b)
LFP#1 Doctor blade-coated
(2 wt.% CB)
C/10
5th
20th
50th
100th
Potential (V) vs Li+/Li
Specific Capacity (mAh/g)
(c)
LFP#1 3D-printed
(2 wt.% CB)
C/10
5th
20th
50th
100th
Potential (V) vs Li+/Li
Specific Capacity (mAh/g)
(d)
LFP#1 Doctor blade-coated
(2 wt.% CB)
C/10
5th
20th
50th
100th
Potential (V) vs Li+/Li
Specific Capacity (mAh/g)
(e)
LFP#1 3D-printed
(2 wt.% CB)
Charge
Discharge
C/10
Energy Density (mWh/g)
Cycle
(f)
LFP#1 Doctor blade-coated
(2 wt.% CB)
Charge
Discharge
C/10
Energy Density (mWh/g)
Cycle
(g)
LFP#1 3D-printed
(2 wt.% CB)
Charge
Discharge
C/10
Energy Density (mWh/g)
Cycle
(h)
LFP#1 Doctor blade-coated
(2 wt.% CB)
Charge
Discharge
C/10
Energy Density (mWh/g)
Cycle

◂**Fig. 5** Galvanostatic (dis)charge profiles (**a**–**d**) and energy density evolutions (**e**–**h**) corresponding to the results presented in Fig. 4, C/10 cycling of Li/LFP cells with 4CMC_2PEDOT 3D-printed and doctor blade-coated electrodes. The subplots (**a**, **e**) and (**c**, **g**) represent the best and worst performances recorded for the 3D-printed electrodes. The best and worst performances among the repetitions for doctor blade-coated electrodes are presented in subplots (**b**, **f**) and (**d**, **h**), respectively. The energy density is normalized to the weight of LFP electrode and electrolyte

a capacity retention below 35% while in some repetitions the capacity drops to zero only after tens of cycles.

The preliminary post-mortem analysis of the aged cells reveals that the structure of the 3D-printed electrodes is well preserved after long-term cycling (Fig. 4d, Fig. S8). A comprehensive aging analysis of the doctor blade-coated and 3D-printed electrodes needs a dedicated study. However, our preliminary analysis suggests that the electrolyte decomposition at the interface with Li electrode is a major source of capacity loss. The electrolyte decomposition and passivation of the Li electrode continuously raises the internal resistance of the cell and can lead to electrolyte dry-out and ion depletion at some part of the thick LFP electrodes (Fig. 4e). This can eventually isolate some fraction of the LFP particles at far-fetched depths in the thick LFP electrodes and turns them electrochemically inaccessible for Li (de)insertion. This can partly explain why the onset cycle for the visible decline in the capacity of the 3D-printed electrodes is much earlier than that for the doctor-blade-coated electrodes (Fig. 4). The thickness of the 3D-printed electrode is more than 2 times that of the doctor-blade-coated electrode and therefore the effects of the electrolyte degradation and loss manifests faster for the thicker 3D electrodes.

A preliminary test was conducted to approximate the share of Li and electrolyte degradation in the overall aging dynamics of the Li/LFP cells. The C/10 cycling of the Li/LFP cell with 3D-printed “4CMC_2PEDOT” electrode was stopped after 40 cycles and the LFP electrode was recovered to assemble a new coin cell with a fresh Li and electrolyte. The cycling was then resumed to further investigate the aging path of the cell (Fig. S9). As expected, after 10 cycles, the refurbished coin cell gradually recovers ~ 60% of the capacity loss experienced by the original cell. This observation confirms the major role of the Li and electrolyte degradation in the capacity loss of our Li/LFP cells. In this regard, a comprehensive aging investigation of the 3D-printed LFP electrodes should use a full cell configuration by pairing the 3D electrodes with a Li-insertion anode such as graphite. This facilitates the assessment of the aging behavior of the 3D-printed electrodes in the absence of complications introduced by the continuous electrolyte decomposition at Li electrode.

The second source of capacity loss is speculated to be linked with the intra-particle fracture of the LFP electrodes (Fig. 4f, g). The excessive fracture of the secondary LFP aggregates can possibly isolate some primary particles from the electronic percolation network of the electrode and decrease the cell capacity. This intra-particle fracture also explains the decrease of the charge-transfer resistance of the Li/LFP cells over short-term cycling observed in the EIS spectra of the cells (Fig. S6−7).

The performance of the Li-ion cells with the porous electrodes coated by the conventional coating techniques is very sensitive to the drying conditions which is well documented in the literature [65–67]. Previous studies have indicated that high drying temperature causes binder migration to the electrode surface, leading to inhomogeneous binder distribution [65, 68, 69]. This deteriorates the electrochemical properties of the electrode [70]. Furthermore, the elevated temperature (110–130 °C) was reported to promote the segregation of binder and conductive additive [71], resulting in lower adhesion strength between the coated material layer and the current collector [72, 73]. However, such inactive material segregation and poor adhesion strength can be improved by drying the electrode at a temperature lower than 80 °C [71]. Additionally, a high drying temperature and fast drying rate also trigger electrode cracks on thicker electrodes manufactured using water-based solvent [74]. In this regard, further research is essential to explore the possible optimization of the drying conditions for the 3D-printed electrodes. Previous reports on 3D-printed electrodes employ high temperatures to dry the electrodes [18, 21, 75]. In addition to high-temperature drying, freeze-drying is a commonly used drying method to treat water-based 3D-printed electrodes [16, 33, 45, 76].

We performed a preliminary analysis for the impact of drying conditions on the performance of the 4CMC_2PEDOT electrodes. Three different drying conditions were tried, namely vacuum drying at 25 °C, vacuum drying at 120 °C and freeze drying followed by vacuum drying at 25 °C. Despite high LFP loading (27.1 mg/cm^2) and thickness (400 µm), no structural defects were detected irrespective of the drying method (Fig. 6a-c). The rate capability data (Fig. 6d) shows that while the electrodes dried at vacuum oven at 25 °C and 120 °C show comparable performance at low C-rates, freeze-dried electrodes deliver a noticeably lower average capacity at C/10 and C/5. However, at C-rates above C/5, the performance of the electrodes prepared with different drying conditions is very similar (Fig. 6d). This preliminary investigation demonstrates the superior resilience of the 3D-printed electrodes to high drying temperatures in contrast to the conventional coating methods.

Towards the optimization of the rate-performance of the 3D-printed electrodes

The observation of inferior rate capability of the 3D-printed electrodes based on LFP#1 compared to its doctor-blade

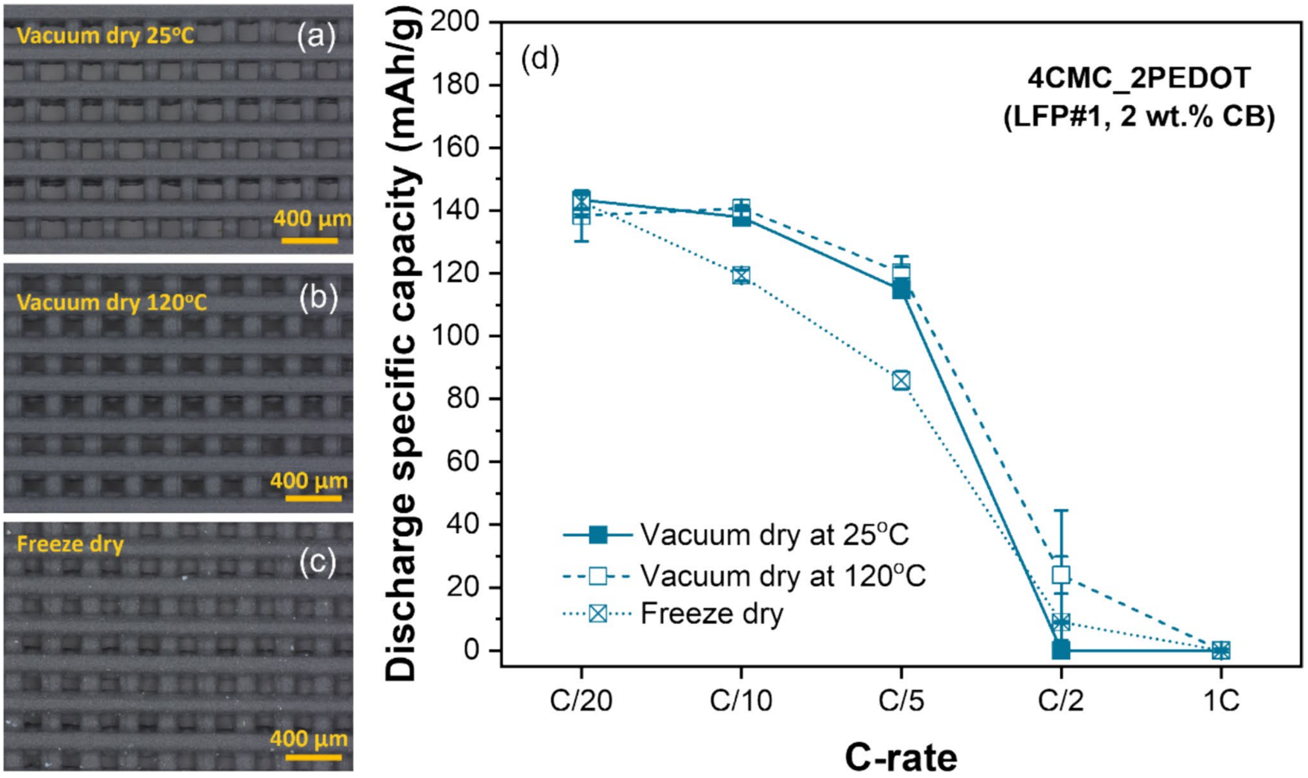

Fig. 6 Optical microscopy images of 4CMC_2PEDOT 3D-printed electrodes prepared with different drying conditions **a** vacuum oven dry at 25 °C, **b** vacuum oven dry at 120 °C, and **c** vacuum freeze dry. **d** Rate capability of the Li/LFP cells as a function of the drying condition

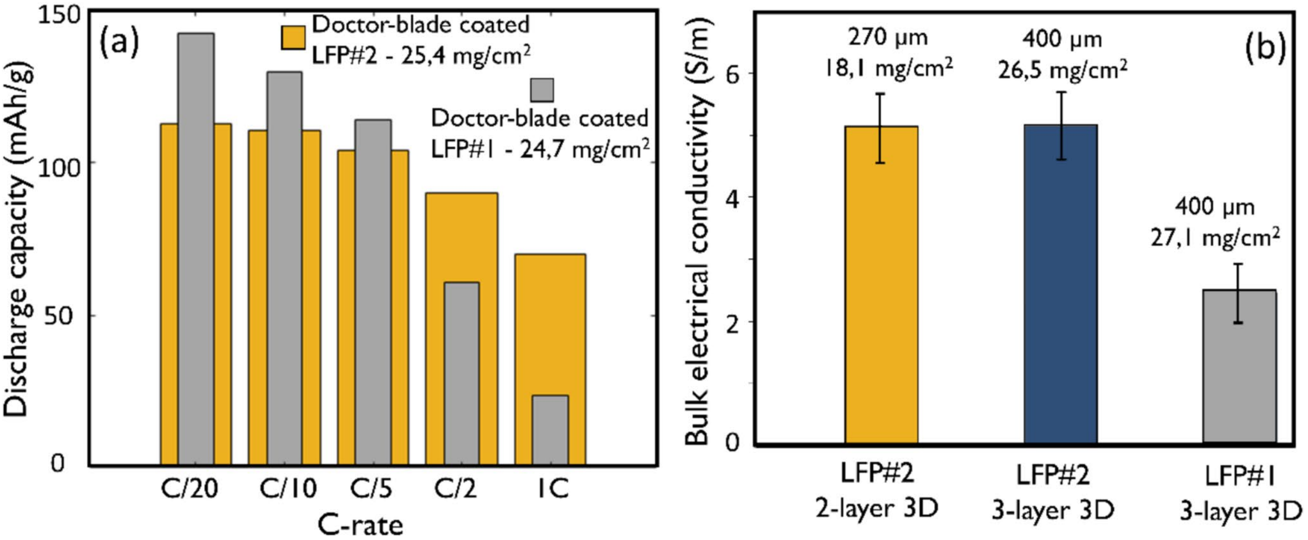

Fig. 7 **a** Comparison of the rate performance of the Li/LFP cells made from two high-loading (~25 mg/cm^2) doctor blade-coated LFP electrodes with the same formulation (4CMC_2PEDOT & 2 wt.% CB) but different types of LFP powders: 4CMC_2PEDOT_DB* and 4CMC_2PEDOT_DB (Table 1), **b** the bulk electrical conductivity of the 3D-printed LFP electrodes compared between the thick 3-layer and thinner 2-layer printed electrodes formulated with the same formulation (4CMC_2PEDOT & 2 wt.% CB) but with different types of LFP and loading: 4CMC_2PEDOT*, 4CMC_2PEDOT, and 4CMC_2PEDOT_thin*

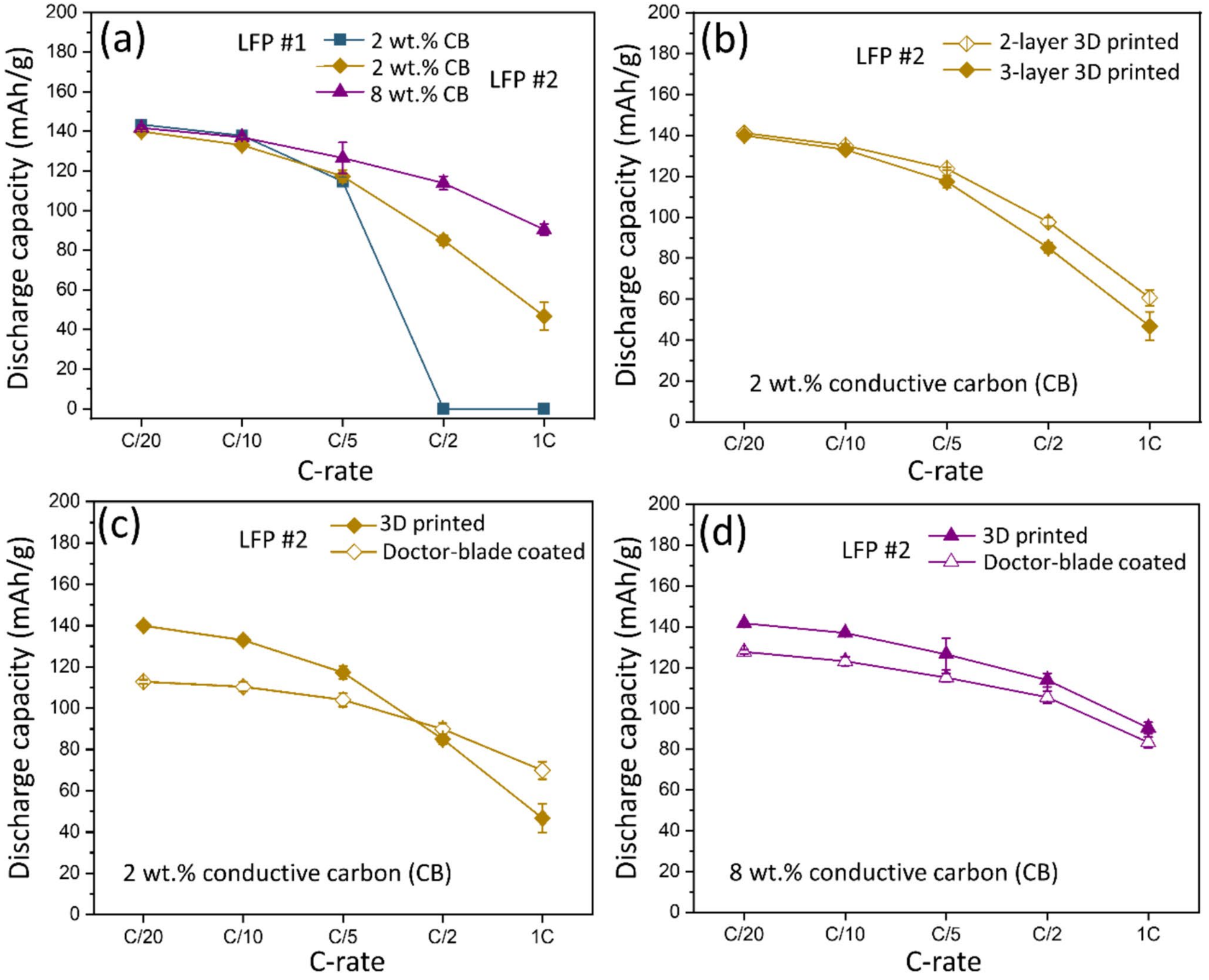

Fig. 8 Rate performance of the Li/LFP cells based on the LFP electrodes formulated with the “4CMC_2PEDOT” binder but with different content of carbon black (CB), type of LFP, and areal loading. **a** Impact of LFP type (LFP#1 vs. LFP#2) and wt.% of carbon black (2 vs 8% wt.%) on the rate performance of the 3D-printed electrodes using the base 3-layer design. **b** Sensitivity of the rate performance to the areal loading of the LFP#2 in 3D-printed electrodes with areal loadings of 18.1 mg/cm^2 (2-layer design, 270 µm) vs. 26.5 mg/cm^2 (3-layer design, 400 µm). **c** 3D-printed LFP#2 electrodes (3-layer design) against its doctor-blade counterpart with 2 wt.% CB, and **d** 8 wt.% CB

counterpart (Fig. 4a) calls for more investigation. A comprehensive optimization of the rate-performance of the 3D-printed electrodes deserves a dedicated study. However, to do so, a preliminary analysis suggests two main adjustable design parameters, namely the properties of the LFP material and the share of the conductive additive in the electrode formulation. Particularly, the impact of intrinsic electronic conductivity of the LFP particles on the rate performance of the 3D-printed electrodes was investigated by using a different source for the LFP powder (Fig. 7). The LFP#2 powder has a higher carbon content (1.7 wt.%) and smaller particle size (100 nm) compared to the LFP#1 (Table 1, experimental section). The discharge capacity of the thick doctor blade-coated LFP#2 electrode is lower compared to the LFP#1 at C-rates below C/2, and higher at C-rates above C/2 (Fig. 7a). This suggests that the LFP#2 is a better candidate for power applications while the LFP#1 is better suited for the energy applications. The higher intrinsic electronic conductivity of the LFP#2 is also reflected in the effective bulk electronic conductivity of the 3D-printed electrodes made thereof (Fig. 7b). The conductivity measurements show that the intra- and inter-fiber electronic conductivity of the 3D-printed electrodes is significantly enhanced by using LFP#2 powders. A high electronic conductivity with LFP#2 sample is observed which is indifferent to the thickness of the 3D printed electrodes in the range of 270–400 µm.

The rate performance of the 4CMC_2PEDOT* 3D-printed electrode formulated with the LFP#2 powder and 2 wt.% CB demonstrates a significant power boost at C/2 and 1 C compared to the LFP#1 (Fig. 8a). Increasing the share of CB conductive additive in the ink formulation is another trivial method to increase the power performance of the 3D-printed electrodes, although this approach is associated with a penalty on the gravimetric energy density of the electrode. Further power enhancement can be achieved with a lower loading of LFP#2 (23.9 mg/cm^2) and a higher share of CB conductive additive, i.e., 8 wt.% CB (Fig. 8a). Decreasing the electrode thickness (400 µm down to 270 µm) while using the base formulation for conductive additives (2 wt.% CB) shows minor improvement to the rate performance of the 3D-printed LFP#2 electrode (Fig. 8b). This observation is in-line with the similar electronic conductivity of the 2-layer and 3-layer 3D electrodes shown earlier in Fig. 7b.

Although the rate performance of the 3D-printed LFP#2 is superior to the LFP#1, it still delivers a lower discharge capacity at 1 C compared to its doctor-blade counterpart (Fig. 8c). At C/2 and 1 C, the rate capability of the 3D-printed LFP#2 with 2% C is lower than its doctor-blade counterpart even when the delivered energy is compared between the two cells (Fig. S10). This suggests that the 2% conductive additive is not enough to secure a competitive electronic charge transport across the 400-µm thickness compared to that in the thinner DB electrode (170 µm). However, the significant inferior performance of the DB-coated electrode at C/20 relative to the 3D-printed electrode suggests that > 20% of LFP particles are disconnected from the charge percolation network and are completely inactive during the (dis)charge of the DB electrode even at a pristine state (Fig. 8c). This observation suggests that in a thick doctor-blade coated electrode there are some LFP particles that are completely shielded likely with a very thick carbon-binder domain and are isolated from the rest of the electrode.

At 2% conductive additive, the 3D electrode is more suitable for energy applications compared to the power applications. This shortcoming, however, can be tackled with the 4CMC_2PEDOT_8CB* electrodes with 8 wt.% of CB (Fig. 8d). This 3D-printed electrode with 23.9 mg/cm^2 loading of LFP#2 outperforms its doctor-blade counterpart over the whole range of C-rate (Fig. 8d). This inferior rate performance of the doctor-blade coated electrode can be partially attributed to the side effects of increasing the CB content in the formulation of the conventionally coated thick electrodes. The thickness of the doctor blade-coated LFP#2 electrode increases from 172 to 210 µm when the CB additive rises from 2 to 8 wt.% to keep a similar areal loading (~ 25 mg/cm^2). This facilitates the manifestation of the long-range transport limitations and showcases the higher performance vulnerability of the electrodes prepared with the traditional coating methods compared to the incremental thickening at higher thicknesses relative to the 3D printing.

The 3D-printed electrodes tested in this research show a competitive performance to their analogous doctor-blade-coated electrodes over the whole range of C-rate in terms of the gravimetric energy density when formulated with 86 wt.% LFP and 8 wt.% CB (Fig. S11). This is similarly the case for the other formulations tested in this study (i.e., 92 wt.% LFP, 2 wt.% CB) but at C-rates up to C/2 (Fig. S10). This is mainly thanks to the better utilization of the loaded mass of the LFP particles which is more uniformly distributed in a 3D-printed electrode compared to a thick electrode coated with a conventional coating technique which is prone to binder migration and significant structural heterogeneity. However, the volumetric energy density of the 3D-printed electrodes is inferior to the doctor-blade-coated electrodes due to their substantially larger thickness. Further optimization in future works is required to fine tune the 3D design of the electrodes, fiber dimensions, electrode porosity, and weight percentage of the conductive additive to strike an optimal balance between the gravimetric and volumetric energy density of the 3D-based cells for a given energy or power application.

Conclusion

In this study, the LFP electrodes with a superior loading as high as 47.1 mg/cm^2 and areal capacity of 4.7 mAh/cm^2 were prepared by DIW 3D-printing at room temperature. The impact of the CMC, PEDOT:PSS, and their mixture as binder was comprehensively investigated on the printability, microstructure, and battery performance of the 3D-printed LFP electrodes. The results showed the constructive synergistic impact of CMC and PEDOT:PSS when used together for obtaining well-printed 3D electrodes. The combination of CMC and PEDOT:PSS improves the mechanical integrity of the electrodes and mitigates the formation of inter- and intra-fiber cracks.

The tortuosity and electrical conductivity measurements of the electrodes revealed that excessive CMC content in the formulation results in high tortuosity and low electrical conductivity, ultimately leading to poor battery performance. In contrast, the PEDOT:PSS decreases the tortuosity and enhances the electrical conductivity and rate capability of the electrodes. Another important finding of this work is that the lower apparent tortuosity of the 3D-printed relative to the conventional electrodes will not necessarily result in the superior performance of the 3D-printed electrodes. The intra-fiber tortuosity in the 3D-printed electrodes can limit the rate performance and needs careful optimization. Moreover, the 3D arrangement of the fibers through- and in-plane of the electrode has a significant impact on the effective electronic conductivity of the 3D-printed electrodes.

Although the non-optimized fiber dimension, microstructure, and 3D arrangements were used in this study, the prepared 3D-printed electrodes demonstrated a superior behavior compared to the doctor blade-coated electrodes. The follow-up studies need to address the challenges relevant to the control of intra-fiber tortuosity and porosity and fiber configurations in the electrode.

Supplementary Information The online version contains supplementary material available at https://doi.org/10.1007/s11581-025-06753-9.

Acknowledgements The authors thank Dirk Vanhoyweghen, Nancy Dewit, and Anne-Marie De Wilde for their help and support in the laboratory, and the characterization of the samples. H. Hamed is grateful to FWO for the financial support via the junior postdoctoral fellowship (12A1R24N). The authors are also grateful to Imerys G & C for providing the carbon black Super-C65, and to Agfa for supplying the Poly(3,4-ethylenedioxythiophene) polystyrene sulfonate (PEDOT:PSS).

Authors' contributions T. N: conceptualization,methodology, investigation, visualization, writing original draft, review & editing H. H: methodology, investigation, visualization, review & editing J. D: methodology, investigation, visualization Y. DV: supervision, methodology, validation, review & editing A. H: validation, investigation, review & editing S. S: supervision, investigation, methodology, validation, review & editing J. L: supervision, conceptualization, methodology, investigation, validation, review & editing M. S: supervision, conceptualization, methodology, validation, writing original draft, review & editing.

Data availability No datasets were generated or analysed during the current study.

Declarations

Competing interests The authors declare no competing interests.

References

1. Patry G, Romagny A, Martinet S, Froelich D (2015) Cost modeling of lithium-ion battery cells for automotive applications. Energy Sci Eng 3:71–82. https://doi.org/10.1002/ese3.47
2. Kuang Y, Chen C, Kirsch D, Hu L (2019) Thick electrode batteries: principles, opportunities, and challenges. Adv Energy Mater 9:1901457. https://doi.org/10.1002/aenm.201901457
3. Parikh D, Christensen T, Li J (2020) Correlating the influence of porosity, tortuosity, and mass loading on the energy density of LiNi0.6Mn0.2Co0.2O2 cathodes under extreme fast charging (XFC) conditions. J Power Sources 474:228601. https://doi.org/10.1016/j.jpowsour.2020.228601
4. Solomon JM, Ahmad SI, Dave A (2022) Ultrafast laser ablation, intrinsic threshold, and nanopatterning of monolayer molybdenum disulfide. Sci Rep 12:6910. https://doi.org/10.1038/s41598-022-10820-w
5. Zheng J, Xing G, Jin L et al (2023) Strategies and challenge of thick electrodes for energy storage: a review. Batteries 9:151. https://doi.org/10.3390/batteries9030151
6. Gallagher KG, Trask SE, Bauer C et al (2016) Optimizing areal capacities through understanding the limitations of lithium-ion electrodes. J Electrochem Soc 163:A138–A149. https://doi.org/10.1149/2.0321602jes
7. Singh M, Kaiser J, Hahn H (2015) Thick electrodes for high energy lithium ion batteries. J Electrochem Soc 162:A1196–A1201. https://doi.org/10.1149/2.0401507jes
8. Long JW, Dunn B, Rolison DR, White HS (2004) Three-dimensional battery architectures. Chem Rev 104:4463–4492. https://doi.org/10.1021/cr020740l
9. Zhang Y, Shi G, Qin J (2019) Recent progress of direct ink writing of electronic components for advanced wearable devices. ACS Appl Electron Mater 1:1718–1734. https://doi.org/10.1021/acsaelm.9b00428
10. Lyu Z, Lim GJH, Koh JJ et al (2021) Design and manufacture of 3d-printed batteries. Joule 5:89–114. https://doi.org/10.1016/j.joule.2020.11.010
11. Qian J, Chen Q, Hong M et al (2022) Toward stretchable batteries: 3d-printed deformable electrodes and separator enabled by nanocellulose. Mater Today 54:18–26. https://doi.org/10.1016/j.mattod.2022.02.015
12. Liu Y, Qiao Y, Zhang Y et al (2018) 3D printed separator for the thermal management of high-performance Li metal anodes. Energy Storage Mater 12:197–203. https://doi.org/10.1016/j.ensm.2017.12.019
13. McOwen DW, Xu S, Gong Y et al (2018) 3D-printing electrolytes for solid-state batteries. Adv Mater 30:1707132. https://doi.org/10.1002/adma.201707132
14. Cheng M, Jiang Y, Yao W et al (2018) Elevated-temperature 3D printing of hybrid solid-state electrolyte for Li-ion batteries. Adv Mater 30:1800615. https://doi.org/10.1002/adma.201800615
15. Ben-Barak I, Ragones H, Golodnitsky D (2022) 3D printable solid and quasi-solid electrolytes for advanced batteries. Electrochem Sci Adv 2:e2100167. https://doi.org/10.1002/elsa.202100167
16. Wang J, Sun Q, Gao X et al (2018) Toward high areal energy and power density electrode for Li-ion batteries via optimized 3D printing approach. ACS Appl Mater Interfaces 10:39794–39801. https://doi.org/10.1021/acsami.8b14797
17. Tao R, Gu Y, Sharma J et al (2023) A conformal heat-drying direct ink writing 3D printing for high-performance lithium-ion batteries. Mater Today Chem 32:101672. https://doi.org/10.1016/j.mtchem.2023.101672
18. De La Torre-Gamarra C, García-Suelto MD, Del Rio Santos D et al (2023) 3D-printing of easily recyclable all-ceramic thick LiCoO2 electrodes with enhanced areal capacity for Li-ion batteries using a highly filled thermoplastic filament. J Colloid Interface Sci 642:351–363. https://doi.org/10.1016/j.jcis.2023.03.117
19. Yee DW, Citrin MA, Taylor ZW et al (2021) Hydrogel-based additive manufacturing of lithium cobalt oxide. Adv Mater Technol 6:2000791. https://doi.org/10.1002/admt.202000791
20. Bao Y, Liu Y, Kuang Y (2020) 3D-printed highly deformable electrodes for flexible lithium ion batteries. Energy Storage Mater 33:55–61. https://doi.org/10.1016/j.ensm.2020.07.010
21. Sun K, Wei T-S, Ahn BY et al (2013) 3D printing of interdigitated Li-ion microbattery architectures. Adv Mater 25:4539–4543. https://doi.org/10.1002/adma.201301036
22. Zhang F, Wu K, Xu X et al (2021) 3D printing of graphite electrode for lithium-ion battery with high areal capacity. Energy Technol 9:2100628. https://doi.org/10.1002/ente.202100628
23. Xu K, Zhao N, Li Y et al (2022) 3D printing of ultrathick natural graphite anodes for high-performance interdigitated three-dimensional lithium-ion batteries. Electrochem Commun 139:107312. https://doi.org/10.1016/j.elecom.2022.107312
24. del-Mazo-Barbara L, Ginebra M-P (2021) Rheological characterisation of ceramic inks for 3D direct ink writing: a review. J Eur Ceram Soc 41:18–33. https://doi.org/10.1016/j.jeurceramsoc.2021.08.031

25. Chen T, Sun A, Chu C et al (2019) Rheological behavior of titania ink and mechanical properties of titania ceramic structures by 3D direct ink writing using high solid loading titania ceramic ink. J Alloys Compd 783:321–328. https://doi.org/10.1016/j.jallcom.2018.12.334
26. Chen H, Ling M, Hencz L et al (2018) Exploring chemical, mechanical, and electrical functionalities of binders for advanced energy-storage devices. Chem Rev 118:8936–8982. https://doi.org/10.1021/acs.chemrev.8b00241
27. Jeon J, Yoo J-K, Yim S et al (2019) Natural-wood-derived lignosulfonate ionomer as multifunctional binder for high-performance lithium-sulfur battery. ACS Sustain Chem Eng 7:17580–17586. https://doi.org/10.1021/acssuschemeng.9b01924
28. Cholewinski A, Si P, Uceda M et al (2021) Polymer binders: characterization and development toward aqueous electrode fabrication for sustainability. Polymers 13:631. https://doi.org/10.3390/polym13040631
29. Hamed H, Yari S, D'Haen J et al (2020) Demystifying charge transport limitations in the porous electrodes of lithium-ion batteries. Adv Energy Mater 10:2002492. https://doi.org/10.1002/aenm.202002492
30. Landesfeind J, Eldiven A, Gasteiger HA (2018) Influence of the binder on lithium ion battery electrode tortuosity and performance. J Electrochem Soc 165:A1122–A1128. https://doi.org/10.1149/2.0971805jes
31. Chou S-L, Pan Y, Wang J-Z et al (2014) Small things make a big difference: binder effects on the performance of Li and Na batteries. Phys Chem Chem Phys 16:20347–20359. https://doi.org/10.1039/C4CP02475C
32. Lux SF, Schappacher F, Balducci A (2010) Low cost, environmentally benign binders for lithium-ion batteries. J Electrochem Soc 157:A320. https://doi.org/10.1149/1.3291976
33. Bao P, Lu Y, Tao P et al (2021) 3D printing PEDOT-CMC-based high areal capacity electrodes for Li-ion batteries. Ionics 27:2857–2865. https://doi.org/10.1007/s11581-021-04063-4
34. Akhlaq M, Mushtaq U, Naz S, Uroos M (2023) Carboxymethyl cellulose-based materials as an alternative source for sustainable electrochemical devices: a review. RSC Adv 13:5723–5743. https://doi.org/10.1039/D2RA08244F
35. Wang Z, Dupré N, Gaillot A-C et al (2012) CMC as a binder in LiNi0.4Mn1.6O4 5V cathodes and their electrochemical performance for Li-ion batteries. Electrochim Acta 62:77–83. https://doi.org/10.1016/j.electacta.2011.11.094
36. Pohjalainen E, Räsänen S, Jokinen M et al (2013) Water soluble binder for fabrication of Li4Ti5O12 electrodes. J Power Sources 226:134–139. https://doi.org/10.1016/j.jpowsour.2012.10.083
37. He M, Yuan L-X, Zhang W-X et al (2011) Enhanced cyclability for sulfur cathode achieved by a water-soluble binder. J Phys Chem C 115:15703–15709. https://doi.org/10.1021/jp2043416
38. Liu C, Cheng X, Li B (2017) Fabrication and characterization of 3D-printed highly-porous 3D LiFePO4 electrodes by low temperature direct writing process. Materials 10:934. https://doi.org/10.3390/ma10080934
39. Eliseeva SN, Kamenskii MA, Tolstopyatova EG, Kondratiev VV (2020) Effect of combined conductive polymer binder on the electrochemical performance of electrode materials for lithium-ion batteries. Energies 13:2163. https://doi.org/10.3390/en13092163
40. Eliseeva SN, Apraksin RV, Tolstopjatova EG, Kondratiev VV (2017) Electrochemical impedance spectroscopy characterization of $LiFePO_4$ cathode material with carboxymethylcellulose and poly-3,4-ethylendioxythiophene/polystyrene sulfonate. Electrochim Acta 227:357–366. https://doi.org/10.1016/j.electacta.2016.12.157
41. Yao Y, Liu N, McDowell MT (2012) Improving the cycling stability of silicon nanowire anodes with conducting polymer coatings. Energy Environ Sci 5:7927. https://doi.org/10.1039/c2ee21437g
42. Nguyen VA, Kuss C (2020) Review—conducting polymer-based binders for lithium-ion batteries and beyond. J Electrochem Soc 167:065501. https://doi.org/10.1149/1945-7111/ab856b
43. Kubarkov AV, Drozhzhin OA, Karpushkin EA et al (2019) Poly(3,4-ethylenedioxythiophene):poly(styrenesulfonic acid)–polymer composites as functional cathode binders for high power LiFePO4 batteries. Colloid Polym Sci 297:475–484. https://doi.org/10.1007/s00396-018-04468-0
44. Michielsen B, Mertens M, De Vos Y (2021) Robocasting of porous alumina hollow fibre monoliths by non-solvent induced phase inversion. Open Ceram 6:100098. https://doi.org/10.1016/j.oceram.2021.100098
45. Gao C, Cui X, Wang C et al (2024) 3D-printed hierarchical porous and multidimensional conductive network based on conducting polymer/graphene oxide. J Materiomics 10:234–244. https://doi.org/10.1016/j.jmat.2023.05.012
46. Li L, Tan H, Yuan X et al (2021) Direct ink writing preparation of *LiFePO4*/MWCNTs electrodes with high-areal li-ion capacity. Ceram Int 47:21161–21166. https://doi.org/10.1016/j.ceramint.2021.04.119
47. Yang L, Gastol D, Kendrick E (2023) Design principles for $LiFePO_4$ electrodes with improved recyclability. Green Chem 25:9959–9968. https://doi.org/10.1039/D3GC03970F
48. Rau DA, Williams CB, Bortner MJ (2023) Rheology and printability: a survey of critical relationships for direct ink write materials design. Prog Mater Sci 140:101188. https://doi.org/10.1016/j.pmatsci.2023.101188
49. Smay JE, Gratson GM, Shepherd RF et al (2002) Directed colloidal assembly of 3D periodic structures. Adv Mater 14:1279–1283. https://doi.org/10.1002/1521-4095(20020916)14:18%3c1279::AID-ADMA1279%3e3.0.CO;2-A
50. Schwab A, Levato R, D'Este M et al (2020) Printability and shape fidelity of bioinks in 3d bioprinting. Chem Rev 120:11028–11055. https://doi.org/10.1021/acs.chemrev.0c00084
51. Glymond D, Vandeperre LJ (2018) Robocasting of MgO-doped alumina using alginic acid slurries. J Am Ceram Soc 101:3309–3316. https://doi.org/10.1111/jace.15509
52. Zhanshayeva L, Favaron V, Lubineau G (2019) Macroscopic modeling of water uptake behavior of PEDOT:PSS films. ACS Omega 4:21883–21890. https://doi.org/10.1021/acsomega.9b02866
53. Ebner M, Chung D-W, García RE, Wood V (2014) Tortuosity anisotropy in lithium-ion battery electrodes. Adv Energy Mater 4:1301278. https://doi.org/10.1002/aenm.201301278
54. Hamed H, Alamooti ZM, Agrawal A et al (2023) Bridging the microstructural evolutions from slurry to porous electrode of a lithium-ion battery. J Energy Chem 84:329–334. https://doi.org/10.1016/j.jechem.2023.05.024
55. Takano T, Masunaga H, Fujiwara A et al (2012) PEDOT nanocrystal in highly conductive PEDOT:PSS polymer films. Macromolecules 45:3859–3865. https://doi.org/10.1021/ma300120g
56. Zhou L, Ning W, Wu C et al (2018) 3D-printed microelectrodes with a developed conductive network and hierarchical pores toward high areal capacity for microbatteries. Adv Mater Technol. https://doi.org/10.1002/admt.201800402
57. Li C-C, Chen C-A, Chen M-F (2017) Gelation mechanism of organic additives with *LiFePO4* in the water-based cathode slurries. Ceram Int 43:S765–S770. https://doi.org/10.1016/j.ceramint.2017.05.315
58. Miller C, Keattch O, Shergill RS, Patel BA (2024) Evaluating diverse electrode surface patterns of 3D printed carbon thermoplastic electrochemical sensors. Analyst 149:1502–1508. https://doi.org/10.1039/D3AN01592K
59. Lang U, Müller E, Naujoks N, Dual J (2009) Microscopical investigations of PEDOT:PSS thin films. Adv Funct Mater 19:1215–1220. https://doi.org/10.1002/adfm.200801258

60. Dupont SR, Novoa F, Voroshazi E, Dauskardt RH (2014) Decohesion kinetics of PEDOT:PSS conducting polymer films. Adv Funct Mater 24:1325–1332. https://doi.org/10.1002/adfm.201302174
61. Zhou J, Anjum DH, Chen L et al (2014) The temperature-dependent microstructure of PEDOT/PSS films: insights from morphological, mechanical and electrical analyses. J Mater Chem C 2:9903–9910. https://doi.org/10.1039/C4TC01593B
62. Heinze T, Koschella A (2005) Carboxymethyl ethers of cellulose and starch – a review. Macromol Symp 223:13–40. https://doi.org/10.1002/masy.200550502
63. Drofenik J, Gaberscek M, Dominko R (2003) Cellulose as a binding material in graphitic anodes for Li ion batteries: a performance and degradation study. Electrochim Acta 48:883–889. https://doi.org/10.1016/S0013-4686(02)00784-3
64. Yi C-W, Kim K (2010) An investigation of $LiFePO_4$/poly(3,4-ethylenedioxythiophene) composite cathode materials for lithium-ion batteries. Bull Korean Chem Soc 31:2698–2700. https://doi.org/10.5012/BKCS.2010.31.9.2698
65. Jaiser S, Müller M, Baunach M et al (2016) Investigation of film solidification and binder migration during drying of Li-ion battery anodes. J Power Sources 318:210–219. https://doi.org/10.1016/j.jpowsour.2016.04.018
66. Wood DL, Li J, Daniel C (2015) Prospects for reducing the processing cost of lithium ion batteries. J Power Sources 275:234–242. https://doi.org/10.1016/j.jpowsour.2014.11.019
67. Yuan C, Deng Y, Li T, Yang F (2017) Manufacturing energy analysis of lithium ion battery pack for electric vehicles. CIRP Ann 66:53–56. https://doi.org/10.1016/j.cirp.2017.04.109
68. Font F, Protas B, Richardson G, Foster JM (2018) Binder migration during drying of lithium-ion battery electrodes: modelling and comparison to experiment. J Power Sources 393:177–185. https://doi.org/10.1016/j.jpowsour.2018.04.097
69. Lippke M, Ohnimus T, Frankenberg F (2024) Drying and calendering of lithium ion battery electrodes: a combined simulation approach. Powder Technol 444:119984. https://doi.org/10.1016/j.powtec.2024.119984
70. Hagiwara H, Suszynski WJ, Francis LF (2014) A raman spectroscopic method to find binder distribution in electrodes during drying. J Coat Technol Res 11:11–17. https://doi.org/10.1007/s11998-013-9509-z
71. Westphal BG, Kwade A (2018) Critical electrode properties and drying conditions causing component segregation in graphitic anodes for lithium-ion batteries. J Energy Storage 18:509–517. https://doi.org/10.1016/j.est.2018.06.009
72. Baunach M, Jaiser S, Schmelzle S (2016) Delamination behavior of lithium-ion battery anodes: influence of drying temperature during electrode processing. Drying Technol 34(4):462–473. https://doi.org/10.1080/07373937.2015.1060497
73. Gören A, Cíntora-Juárez D, Martins P et al (2016) Influence of solvent evaporation rate in the preparation of carbon-coated lithium iron phosphate cathode films on battery performance. Energy Technol 4:573–582. https://doi.org/10.1002/ente.201500392
74. Kumberg J, Müller M, Diehm R et al (2019) Drying of lithium-ion battery anodes for use in high-energy cells: influence of electrode thickness on drying time, adhesion, and crack formation. Energy Technol 7:1900722. https://doi.org/10.1002/ente.201900722
75. Cong M, Du Y, Liu Y et al (2024) Preparation of lithium iron phosphate battery by 3D printing. Ceram Int 50:14749–14756. https://doi.org/10.1016/j.ceramint.2024.01.389
76. Liu C, Xu F, Liu Y et al (2019) High mass loading ultrathick porous Li4Ti5O12 electrodes with improved areal capacity fabricated via low temperature direct writing. Electrochim Acta 314:81–88. https://doi.org/10.1016/j.electacta.2019.05.082